

Analysis of the Degree of Nematic Ordering within Dense Aqueous Dispersions of Charged Anisotropic Colloids by ^{23}Na NMR Spectroscopy

Patrice Porion,* Anne Marie Faugère, and Alfred Delville

Centre de Recherche sur la Matière Divisée CNRS, 1b rue de la Férollerie, 45071 Orléans Cedex 02, France

Received: June 15, 2005; In Final Form: August 20, 2005

Aqueous dispersions of Laponite, a synthetic clay neutralized by sodium counterions, are used as a model of charged anisotropic colloids to probe the influence of the shape of the particle on their organization within a macroscopic nematic phase. Because of the large fraction of condensed sodium counterions in the vicinity of the clay particle, ^{23}Na NMR is a sensitive probe of the nematic ordering of the clay dispersions. We used line shape analysis of the ^{23}Na NMR spectra and measurements of the Hahn echo attenuation to quantify the degree of alignment of the individual clay particles along a single nematic director. As justified by simple dynamical simulations of the interplay between the sodium quadrupolar relaxation and its diffusion through the porous network limited by the surface of the clay particles, we probe the degree of ordering within these clay nematic dispersions by measuring the variation of the apparent ^{23}Na NMR relaxation rates as a function of the macroscopic orientation of the clay dispersion within the magnetic field.

I. Introduction

In the past decade, the organization of dispersions of anisotropic colloids of any shape (rods, disks, ellipsoids) was the subject of numerous experimental^{1–20} and numerical^{21–30} studies, mainly focused on the isotropic/nematic phase transition. In that framework, the influence of various parameters has been investigated (shape, aspect ratio) but also including external forces (flow,³¹ shearing,³² gravity,³³ magnetic field^{34–37}). Since the pioneering work of Onsager,³⁸ a first-order isotropic/nematic phase transition is predicted to occur within the dispersions of such anisotropic rigid particles because of some compensation between the diffusional and rotational entropy. This prediction was confirmed by numerous experimental^{2,3,9–14} and numerical^{21–27} observations performed on various dispersions of rigid anisotropic particles. However, a question still remains unresolved: What is the influence of the long-range electrostatic coupling on the balance between these entropic contributions to the free energy of the dispersion? Various numerical simulations have indeed demonstrated that the electrostatic repulsion between charged rods³⁹ or disks^{40,41} favors a perpendicular orientation, while the excluded volume interaction favors a parallel alignment. Do these dispersions of charged anisotropic colloids still exhibit an isotropic/nematic phase transition and of which order?

We studied the organization within aqueous dispersions of Laponite,^{1–7} a synthetic clay, because these charged colloidal particles have a high chemical purity and are well characterized.^{42–43} Clays constitute a large class of natural materials, resulting from the layering of metallic oxides. Because of their various physicochemical properties (high specific surface, important electric surface charge, swelling, flocculation), they are used in many industrial applications (adsorbent, waste storing, ionic exchanger, food and cosmetic industry, water treatment). Synthetic Laponite results from the sandwiching of one layer of magnesium oxides, with octahedral coordination, between two layers of silicium oxides, with tetrahedral coordination.

In dilute aqueous dispersions, Laponite appears as isolated rigid disks (diameter ~ 300 Å, thickness 10 Å)⁴³ neutralized by 1000 exchangeable sodium counterions. The negative charge of these particles results from substitution of some magnesium from the octahedral network by lithium. Because of the strong condensation of the sodium counterions in the electrostatic well in the vicinity of the clay surface, 50% of the neutralizing sodium counterions are localized near to the clay surface.⁴¹ They are thus ideal probes to measure the structural and dynamical properties of the clay dispersions.

^{23}Na NMR spectroscopy is a powerful tool to perform such studies because the line shape and the relaxation rates of this spin $3/2$ nucleus were already shown to be sensitive probes of the structure of the solid/liquid interfaces^{44,45} and of the dynamical properties^{46,47} of the counterions neutralizing various polyions. As an example, ^{23}Na NMR was already used to detect the isotropic/nematic transition within Laponite dispersions.⁴⁴ Since the measured quadrupolar splitting, a fingerprint of the nematic ordering of the clay dispersion, is also an increasing function of the fraction of condensed sodium counterions, it cannot be used alone as an intrinsic probe of the degree of nematic ordering as a function of the clay concentration. The purpose of this study is to extract complementary information on the degree of ordering of the clay dispersions by analyzing the NMR relaxation behavior of the sodium counterions. The intrinsic ^{23}Na relaxation rates, evaluated in a frame attached to the clay dispersion,⁴⁸ are extracted from the apparent ^{23}Na relaxation rates measured as a function of the angle between the nematic director of the dispersion and the static magnetic field. As illustrated by numerical simulations of the ion diffusion and relaxation, the difference between these intrinsic relaxation rates is a probe of the degree of nematic ordering. The gradual increase of that difference as a function of the clay concentration is a qualitative measurement of the progressive ordering of the dispersion, independent of any variation of the fraction of condensed sodium counterions. The same analysis may be applied to dispersions of any class of charged anisotropic colloids neutralized by quadrupolar counterions.

* To whom correspondence should be addressed. E-mail: porion@cirs-orleans.fr.

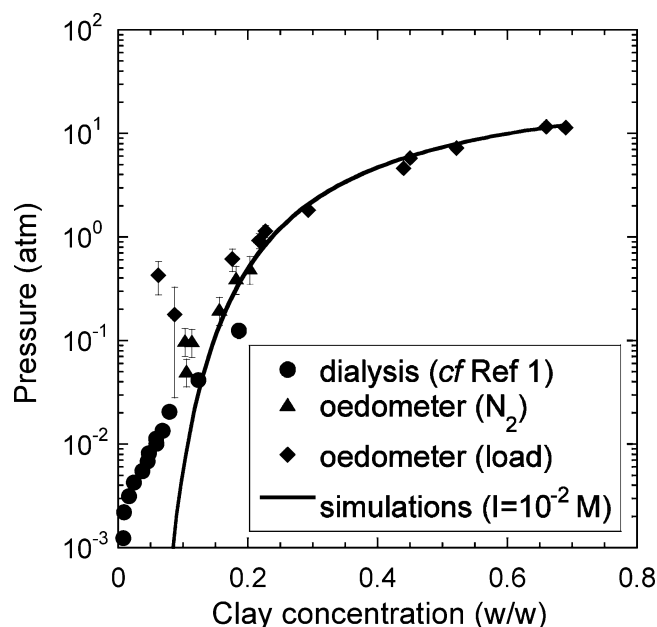


Figure 1. Equation of state of the Laponite dispersion at an ionic strength 10^{-2} M either measured by dialysis¹ or measured by oedometric compression performed by using a piston^{44,45} or inert gas (N_2).

II. Material and Methods

A. Sample Preparation. Laponite RD was purchased from Laporte and used without purification. Dilute Laponite dispersions (less than 3% w/w) were prepared by stirring in an electrolyte solution ($NaCl$ 10^{-2} M, $NaOH$ 10^{-4} M) to prevent the dissolution⁴² of the clay particles. Concentrated samples (up to 92% w/w) were obtained by uniaxial compression using either a piston with an external load or N_2 pressure in order to avoid the friction between the cylinder of the oedometer and its piston. A filtration membrane ($0.1 \mu m$ from osmonics) was used to extract the excess solvent during the compression without particle loss. The final concentration of the dense clay dispersions was determined by measuring the water loss of the sample under vacuum at $80^\circ C$. The samples mechanically compressed by using an external load remained simply in equilibrium with their eluate through the dialysis membrane. This procedure was shown to weakly modify⁴⁵ the ionic strength of the solvent reservoir in equilibrium^{49,50} with the dispersion. By contrast, an external solvent reservoir of fixed ionic strength was used to replace the eluate of the dense samples prepared under N_2 compression. Figure 1 displays the resulting equation of state confirming the order of magnitude of the pressure loss (~ 0.3 atm) due to friction forces⁴⁵ and the equivalence between both procedures above that limiting pressure. At clay concentrations larger than 0.18 w/w, the measured equation of state of the Laponite dispersion agrees well with the predictions of the diffuse layer theory in the framework of the cell model^{49,50} for a very simple geometry: two infinite and parallel charged lamellae, bearing the same surface charge density as the Laponite clay ($7 \times 10^{-3} e/\text{\AA}^2$). The discrepancy detected below that limiting concentration results probably from the disorder within the dispersions of real clay particles due to their finite size (diameter 300 \AA , thickness 10 \AA).⁴³

B. NMR Measurements. 1. Experimental Conditions. ^{23}Na spectra and relaxation measurements were obtained on a DSX360 Bruker spectrometer, with a static magnetic field B_0 of 8.465 T. A broad spectral width (1 MHz) was used, corresponding to a fast acquisition procedure (dwell time $1 \mu s$) in order to detect the fast attenuation ($R_2^{\text{fast}} \sim 4 \times 10^4 s^{-1}$) and

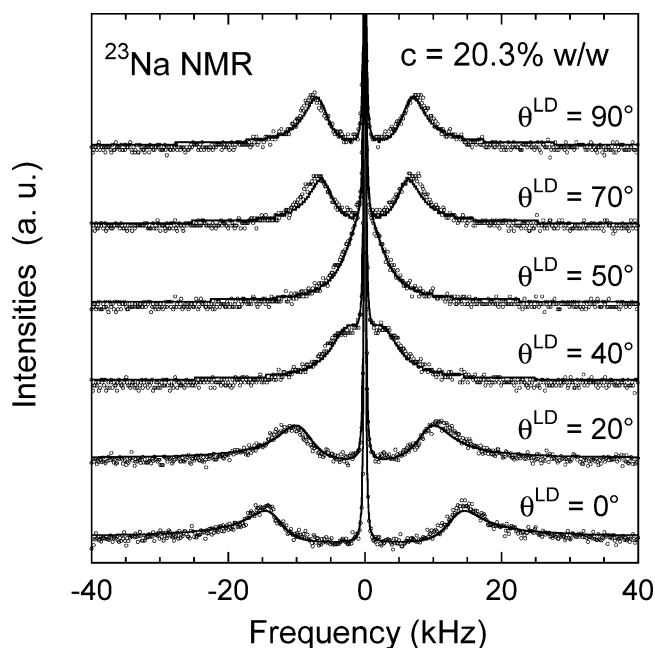


Figure 2. Illustration of the line shape analysis (see text) performed for a Laponite dispersion 20.3% w/w.

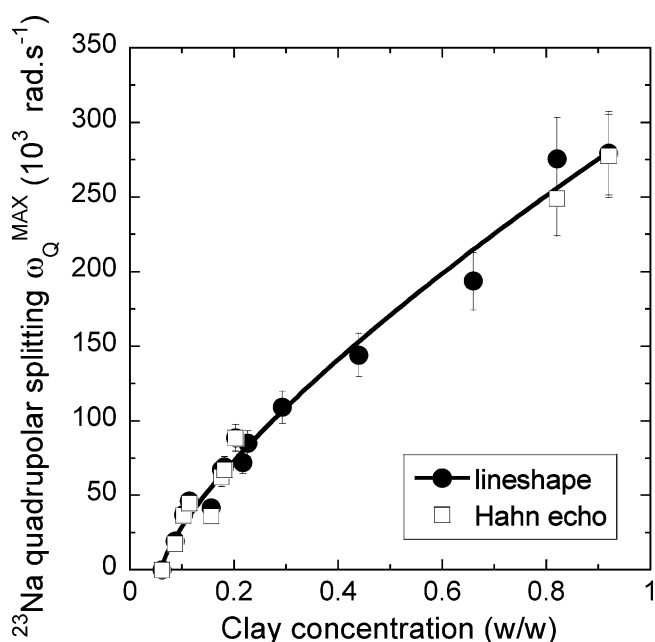


Figure 3. Variation of the ^{23}Na maximum quadrupolar splitting as a function of the clay concentration determined by the line shape analysis or the Hahn echo attenuation.

the large quadrupolar residual splitting ($\omega_Q \sim 3 \times 10^5 \text{ rad}\cdot\text{s}^{-1}$) of the sodium counterions within these dense clay dispersions. To prevent the signal loss, the delay between the detection pulse and the signal acquisition was reduced to its minimal value ($\tau = 4.5 \mu s$). The pulse duration necessary to tilt the magnetization into the transverse detection plane was typically on the order of magnitude of $10 \mu s$. The residual splitting and the different components of the transverse relaxation rates of the sodium nuclei were deduced by two independent procedures: the line shape analysis (cf Figure 2) recorded after a single pulse and the echo attenuation (cf Figure 7) measured after the Hahn^{51,52} pulse sequence.

The ^{23}Na spectra were recorded by using a homemade receiver. A solenoid coil was prepared by wrapping a copper

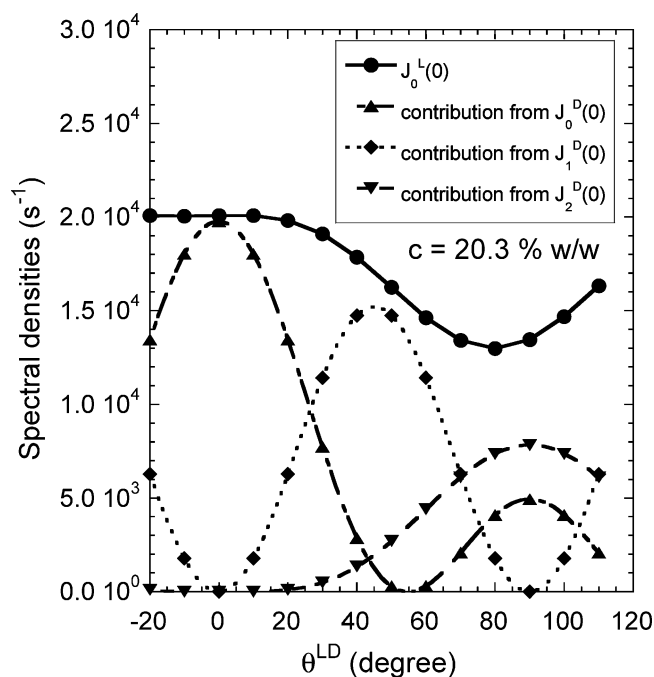


Figure 4. Angular variation of the apparent spectral density ($J_0^L(0)$) in addition to its three contributions from the intrinsic spectral densities ($J_m^D(0)$ with $m = 0-2$) evaluated in a frame attached to the dispersion (see text).

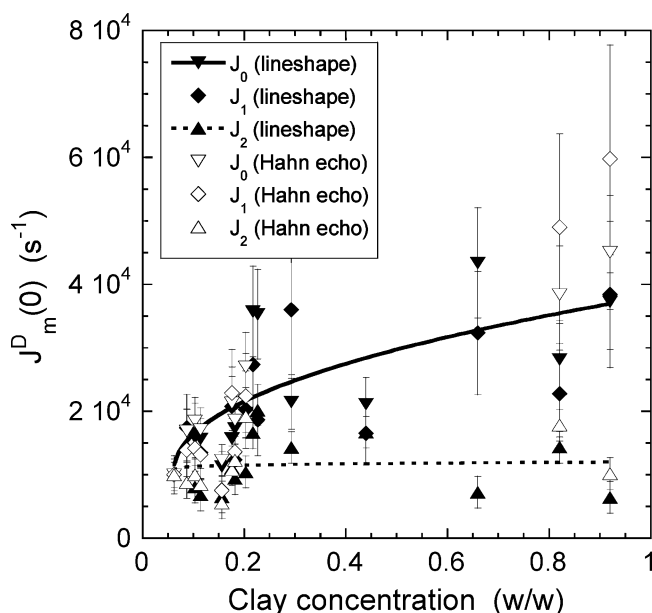


Figure 5. Variation of the intrinsic spectral densities obtained from the angular variation of the apparent spectral densities obtained from the line shape analysis and the Hahn echo attenuation (see text).

wire onto the grooves cut on a Teflon tube (2.8 mm thickness, 8.4 mm internal diameter). The sample holder is cut inside a Teflon cylinder fitting the inner cavity of the tube bearing the coil to optimize its receptivity. The rotational axis of the sample holder coincides with the cylindrical axis of the radio frequency coil and is thus perpendicular to the static magnetic field. Thanks to graduations on the tube bearing the coil, the angle between the static magnetic field and a normal to the cylindrical axis of the sample holder is measured with an accuracy of better than 5°. After compression of the dispersions, the dense clay samples were cut in order to fill the sample holder. The compression axis of the dense clay sample is set perpendicular to the

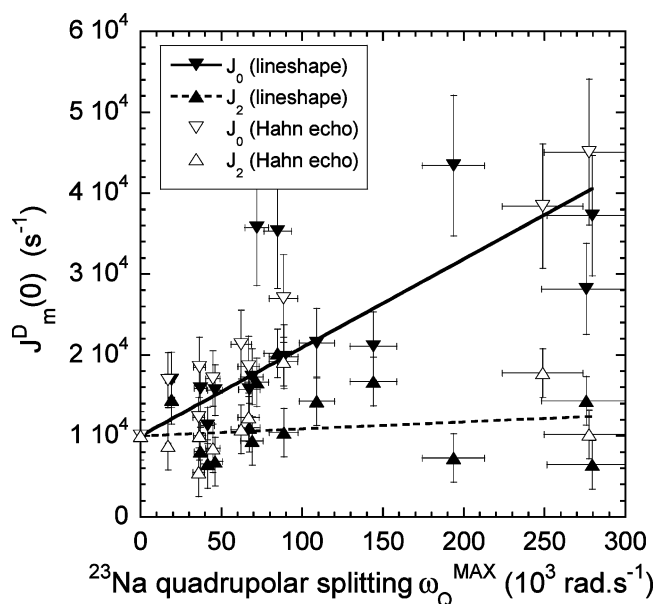


Figure 6. Correlation between the intrinsic spectral densities and the maximum quadrupolar splitting indicating a gradual increase of the difference between $J_0^D(0)$ and $J_2^D(0)$ as a function of the clay concentration.

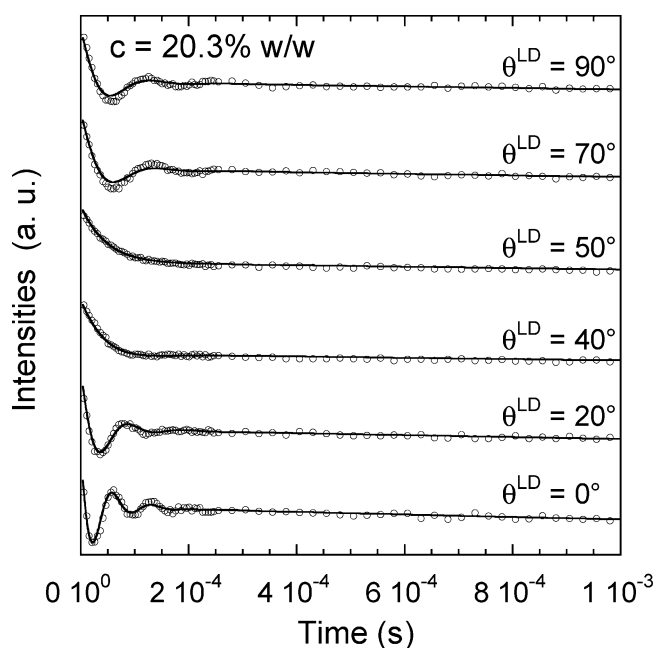


Figure 7. Illustration of the agreement between the measured Hahn echo attenuation and the calculated values by solving eqs 7–14 (see text).

cylindrical axis of the sample holder, and the initial angle ($\theta^{\text{LD}} = 0^\circ$) corresponds to an orientation of the compression axis of the dense clay sample parallel to the static magnetic field.

2. Static Quadrupolar Coupling. The quadrupolar Hamiltonian is defined by^{51–57}

$$H_Q = \sqrt{\frac{3}{2}} \frac{eQ(1 + \gamma_\infty)}{I(2I - 1)\hbar} \sum_{p=-2}^2 (-1)^p F_{2,-p}^L T_{2,p} \quad (1a)$$

where Q is the quadrupolar moment of the nuclei ($0.11 \times 10^{-28} \text{ m}^2$ for ^{23}Na),⁵⁸ and $(1 + \gamma_\infty)$ is the Steinhermer antishielding factor (5.1 for sodium)⁵⁸

$$\begin{aligned}
F_{2,0}^L &= \frac{1}{2} V_{zz}^L \\
F_{2,\pm 1}^L &= \mp \frac{1}{\sqrt{6}} (V_{xz}^L \pm iV_{yz}^L) \\
F_{2,\pm 2}^L &= \frac{1}{2\sqrt{6}} (V_{xx}^L - V_{yy}^L \pm 2iV_{xy}^L)
\end{aligned} \quad (1b)$$

and

$$\begin{aligned}
T_{2,0} &= \frac{1}{\sqrt{6}} (3I_z^2 - I(I+1)) \\
T_{2,\pm 1} &= \mp \frac{1}{2} (I_{\pm} I_z + I_{\pm} I_z) \\
T_{2,\pm 2} &= \frac{1}{2} I_{\pm}^2
\end{aligned} \quad (1c)$$

$V_{\alpha\beta}^L$ are the components of the electrostatic field gradient evaluated in the laboratory frame (noted L). I_x , I_y , and I_z are the spin operators and $I_{\pm} = I_x \pm iI_y$. In the presence of a static quadrupolar coupling, the equidistant Zeeman energy levels are modified by the residual quadrupolar coupling whose first-order approximation gives

$$\bar{H}_Q^1 = \frac{eQ(1 + \gamma_{\infty})}{4I(2I - 1)\hbar} \langle V_{zz}^L \rangle (3m^2 - I(I + 1)) \quad (2)$$

leading to a quadrupolar splitting of the resonance lines according to

$$\begin{aligned}
\omega_{m-1,m} &= \frac{3eQ(1 + \gamma_{\infty})}{4I(2I - 1)\hbar} \langle V_{zz}^L \rangle (1 - 2m) \\
&\text{for } m \text{ varying between } I \text{ and } -I + 1
\end{aligned} \quad (3)$$

During a change of frame, the components of the field gradients transform like the second-order spherical harmonics^{48,52}

$$F_{2,q}^L = \sum_{p=-2}^2 F_{2,p}^D D_{p,q}^{LD}(\theta, \varphi, \psi) \quad (4)$$

where $D_{p,q}^{LD}(\theta, \varphi, \psi)$ are the components of the Wigner rotation matrix^{48,52} defined by the set of (θ, φ, ψ) Euler angles. In the system under study, three sets of frames must be considered: the laboratory frame (noted L), a frame attached to the dense clay dispersion (noted D), and finally a set of frames fixed to the each clay particle (noted P) and corresponding to the eigenvectors of the matrix describing the electrostatic field gradient felt by the condensed sodium counterions. The \vec{e}_z directors of these different frames are, respectively, the direction of the static magnetic field B_0 (laboratory frame L), the direction of the nematic director (dispersion frame D), and the directors of the principal component of the electrostatic field gradient (particle frame P). A molecular modeling of the clay/water interface was used previously⁴⁶ to evaluate, in the frame attached to the clay particle (noted P), the residual quadrupolar coupling felt by the sodium counterions condensed at the surface of the clay particle ($V_{zz}^B = \langle V_{zz}^P \rangle \approx 7 \times 10^{19}$ V/m²) with $\eta_Q = 0$ (η_Q is the asymmetry parameter defined as $\eta_Q = (V_{xx} - V_{yy})/V_{zz}$), according to the numerical uncertainty.⁴⁶ The average distortion of the hydration shell of the condensed sodium counterions induced by the charged solid/liquid interface (i.e., the clay surface) is responsible for this residual quadrupolar splitting. As a consequence, the principal axis corresponding to this

residual quadrupolar coupling was shown to coincide⁴⁶ with that normal to the clay surface.

In the framework of a simple two-state model, we assume the coexistence between only two spin populations corresponding to the free and the condensed sodium counterions, respectively, with a fast exchange between these two spin populations. This hypothesis is in complete agreement with the temperature variation of the ²³Na longitudinal relaxation rate measured within these clay dispersions.⁴⁴ As a consequence, by using eqs 3–4, one deduces the measured quadrupolar splitting

$$\begin{aligned}
\omega_Q^{\text{app}} &= p_F \omega_Q^F + p_B \omega_Q^B = \\
&A_Q p_B V_{zz}^B \sum_{p=-2}^2 D_{p,0}^{LD}(\theta^{\text{LD}}, \varphi^{\text{LD}}, \psi^{\text{LD}}) \langle D_{0,p}^{\text{DP}}(\theta^{\text{DP}}, \varphi^{\text{DP}}, \psi^{\text{DP}}) \rangle
\end{aligned} \quad (5)$$

where p_F and p_B are the fraction of free and condensed sodium counterions, respectively, and $A_Q = (eQ(1 + \gamma_{\infty})/(2\hbar))$ for spin ^{3/2} nuclei. The angular average is evaluated in eq 5 over all the orientations of the clay particles within the dispersion. The environment of the free sodium cations is isotropic ($\omega_Q^F = 0$). The first Wigner rotation matrix describes the orientation of the macroscopic clay sample with respect to the static magnetic field, and the last factor characterizes the average orientation of the clay particles within the dispersion. For clay dispersions with cylindrical symmetry, only the component $p = 0$ contributes to eq 5 which reduces to

$$\omega_Q^{\text{app}} = A_Q p_B V_{zz}^B \frac{3 \cos^2 \theta^{\text{LD}} - 1}{2} \left\langle \frac{3 \cos^2 \theta^{\text{DP}} - 1}{2} \right\rangle \quad (6)$$

As a consequence, the intrinsic splitting characterizing the clay dispersion is the maximum splitting measured when the nematic director of the dispersion coincides with the direction of the static magnetic field. However, it is not an absolute measurement of the degree of ordering of the clay dispersion ($\langle (3 \cos^2 \theta^{\text{DP}} - 1)/2 \rangle$) because of the possible variation of the fraction of condensed sodium counterions (p_B) as a function of clay concentration.

3. Quadrupolar Relaxation. In the framework of the Redfield theory,^{50–57} the relaxation of the quadrupolar nuclei is related to the fluctuating part of the quadrupolar coupling, by using the master equation

$$\frac{d\sigma^*}{dt} = -i[H_S^*, \sigma^*] + f(\sigma^*) \quad (7)$$

where H_S^* is the static Hamiltonian including the residual static quadrupolar Hamiltonian and the Hamiltonian describing the radio frequency pulse; $H_{\text{QF}}^*(t)$ is the fluctuating component of the quadrupolar Hamiltonian. All calculations are performed in the Larmor frequency rotating frame, as indicated by the asterisk. The last term of eq 7 describes the contribution from the fluctuating part of the quadrupolar coupling^{53–57}

$$f(\sigma^*) = - \int_0^t \langle [H_{\text{QF}}^*(t), [e^{-iH_S^* \tau} H_{\text{QF}}^{*+}(t - \tau) e^{iH_S^* \tau} \sigma^*(t)]] \rangle d\tau \quad (8)$$

The fluctuating component of the quadrupolar Hamiltonian is written for spin ^{3/2} nuclei

$$H_{\text{QF}}^*(t) = C_Q \sum_{m=-2}^2 (-1)^m \hat{T}_{2,m} e^{im\omega_Q t} (F_{2,-m}^L(t) - \langle F_{2,-m}^L(t) \rangle) \quad (9)$$

with

$$C_Q = \frac{eQ(1 + \gamma_\infty)}{\hbar}$$

The orthonormal tensor operators⁵⁹ ($\hat{T}_{l,m} = a_l T_{l,m}$, with $a_0 = 1/2$, $a_1 = 1/\sqrt{5}$, $a_2 = 1/\sqrt{6}$, and $a_3 = \sqrt{2}/3$ for $l = 3/2$) are used as a complete basis set to solve eqs 7–9 in order to calculate the time evolution of the different coherences. Symmetric and antisymmetric combinations of the operators are also introduced

$$\begin{aligned}\hat{T}_{l,m}(s) &= \frac{1}{\sqrt{2}} (\hat{T}_{l,-m} + \hat{T}_{l,m}) \\ \hat{T}_{l,m}(a) &= \frac{1}{\sqrt{2}} (\hat{T}_{l,-m} - \hat{T}_{l,m})\end{aligned}\quad (10)$$

simplifying the notations of the transverse component of the magnetization

$$I_x = \sqrt{5} \hat{T}_{1,1}(a) \quad (11)$$

while the residual quadrupolar Hamiltonian reduces to

$$H_{QS} = \frac{\omega_Q}{6} (3I_z^2 - I(I+1)) = \omega_Q \hat{T}_{2,0} \quad (12)$$

For spin $3/2$ nuclei, 16 spin operators⁵⁹ represented by irreducible tensors are required to fully describe the spin dynamics by including the identity ($\hat{T}_{0,0}$), the longitudinal ($\hat{T}_{1,0}$), and transverse ($\hat{T}_{1,1}(s)$, $\hat{T}_{1,1}(a)$) components of the magnetization, the quadrupolar spin polarization ($\hat{T}_{2,0}$), the second-order single-quantum coherences ($\hat{T}_{2,1}(s)$, $\hat{T}_{2,1}(a)$), the second-order double-quantum coherences ($\hat{T}_{2,2}(s)$, $\hat{T}_{2,2}(a)$), the octopolar spin polarization ($\hat{T}_{3,0}$), the third-order single-quantum coherences ($\hat{T}_{3,1}(s)$, $\hat{T}_{3,1}(a)$), the third-order double-quantum coherences ($\hat{T}_{3,2}(s)$, $\hat{T}_{3,2}(a)$), and the third-order triple-quantum coherences ($\hat{T}_{3,3}(s)$, $\hat{T}_{3,3}(a)$). By assuming that the decorrelation of the fluctuating part of the quadrupolar Hamiltonian occurs at a time scale much shorter than that corresponding to the evolution of the different coherences, one can extend to infinity the upper limit in the integral of eq 8, leading to a set of linear differential equations which may be translated into matrix form. More details are given in the literature.^{53–57} Through the calculation of the eigenvalues and eigenvectors of the resulting evolution and relaxation matrixes, it is then possible to simulate the magnetization of spin $3/2$ nuclei detected either after a single pulse, to simulate the line shape of the ^{23}Na NMR spectrum, or during the Hahn pulse sequence used to measure the attenuation of the echo (T_2 measurement). By using a numerical procedure, we are able to solve the set of eqs 7–12 and simulate the time evolution⁴⁴ of the different coherences during any sequence of pulse by starting from an equilibrium longitudinal magnetization. The only parameters required to perform this numerical treatment are the residual quadrupolar splitting, the apparent spectral densities, and the experimental parameters characterizing the pulse itself (i.e., its intensity, duration, and phase). The line shape of the ^{23}Na NMR spectra is evaluated after numerical Fourier transform of the simulated free induction decay (FID) signal. In the presence of a static quadrupolar coupling, this procedure is required to describe the ^{23}Na NMR spectrum obtained after Fourier transform of the FID which exhibits, among other things, a depletion of the baseline around the central resonance (see Figure 2, for $\theta^{\text{LD}} = 0^\circ$). This is due to the fact that the FID is not a simple superposition of damped sine functions but involves coherence transfers^{60,61} which occur during the evolution of the

transverse magnetization. Of course, these transfers depend on the relaxation parameters (i.e., spectral densities).

By combining eqs 7–12, one can note that the time evolution of the different coherences contained in σ^* will be proportional to the Fourier transform of the memory functions describing the decorrelation of the fluctuating part of the quadrupolar Hamiltonian⁵¹

$$\begin{aligned}G_m^L(\tau) &= \langle (F_{2,m}^L(0) - \langle F_{2,m}^L \rangle) (F_{2,-m}^L(\tau) - \langle F_{2,-m}^L \rangle) \rangle + \\ &\quad \langle (F_{2,-m}^L(0) - \langle F_{2,-m}^L \rangle) (F_{2,m}^L(\tau) - \langle F_{2,m}^L \rangle) \rangle\end{aligned}\quad (13)$$

By the use of the Wigner rotation matrixes (cf eq 4), it is possible to relate the derivation of these *apparent* correlation functions evaluated in the laboratory frame⁴⁸ (noted L) to their *intrinsic* value evaluated in the frame attached to the clay dispersion (noted D)

$$\begin{aligned}G_0^L(\tau) &= \frac{1}{4} (1 - 3 \cos^2 \theta^{\text{LD}})^2 G_0^D(\tau) + \\ &\quad 3 \cos^2 \theta^{\text{LD}} \sin^2 \theta^{\text{LD}} G_1^D(\tau) + \frac{3}{4} (1 - \cos^2 \theta^{\text{LD}})^2 G_2^D(\tau)\end{aligned}\quad (14a)$$

$$\begin{aligned}G_1^L(\tau) &= \frac{3}{2} \cos^2 \theta^{\text{LD}} \sin^2 \theta^{\text{LD}} G_0^D(\tau) + \frac{1}{2} (1 - 3 \cos^2 \theta^{\text{LD}} + \\ &\quad 4 \cos^4 \theta^{\text{LD}}) G_1^D(\tau) + \frac{1}{2} (1 - \cos^4 \theta^{\text{LD}}) G_2^D(\tau)\end{aligned}\quad (14b)$$

$$\begin{aligned}G_2^L(\tau) &= \frac{3}{8} (1 - \cos^2 \theta^{\text{LD}})^2 G_0^D(\tau) + \frac{1}{2} (1 - \cos^4 \theta^{\text{LD}}) G_1^D(\tau) + \\ &\quad \frac{1}{8} (1 + 6 \cos^2 \theta^{\text{LD}} + \cos^4 \theta^{\text{LD}}) G_2^D(\tau)\end{aligned}\quad (14c)$$

Since

$$J_m^X(m\omega_0) = 3C_Q^2 \int_{-\infty}^{\infty} G_m^X(\tau) e^{im\omega_0\tau} d\tau \quad (15)$$

with $X = L, D$, or P , the same linear combinations are used to determine the apparent spectral densities ($J_m^L(m\omega_0)$) from the intrinsic spectral densities evaluated in the frame attached to the clay sample ($J_m^D(m\omega_0)$), explaining the variation of the apparent relaxation rates as a function of the orientation of the clay sample into the magnetic field.^{48,62–64} Obviously, within isotropic clay dispersions, all the memory functions $G_m^D(\tau)$ coincide and the measured relaxation rates are independent of the sample orientation.

For spin $3/2$ nuclei under residual quadrupolar coupling, the central resonance line, which corresponds to the $-1/2 \leftrightarrow 1/2$ transition, represents 40% of the total magnetization with a transverse relaxation rate given by $R_2^{\text{slow}} = J_1^L(\omega_0) + J_2^L(2\omega_0)$. The two satellites, corresponding to the $-3/2 \leftrightarrow -1/2$ and the $1/2 \leftrightarrow 3/2$ transitions, represent 60% of the total magnetization with a transverse relaxation rate given by $R_2^{\text{fast}} = J_0^L(0) + J_1^L(\omega_0)$.

C. Numerical Simulations. Simple numerical simulations of Brownian dynamics were performed to analyze the influence of the degree of organization of the clay dispersion on the relaxation behavior of its neutralizing sodium counterions. For that purpose, 466 rigid disks (diameter 300 Å, thickness 10 Å) were distributed in a cubic box (length 0.14 μm) by using only hard core repulsion to model dense dispersions of Laponite clay (concentration 0.32 w/w). Nematic dispersions of the controlled degree of ordering were generated by selecting the orientation of the clay disks in order to sample uniformly the function $\cos \theta^{\text{DP}}$ between 1 and a minimum value (where θ^{DP} is the angle

between the nematic director and the vector normal to the clay surface, see above). Four limiting values were selected: $(\cos \theta^{\text{DP}})_{\min} = 0.931, 0.894, 0.856$, and 0.816 , corresponding to a minimum value of the order parameter $P_2^{\min} = (3(\cos \theta^{\text{DP}})^2_{\min} - 1)/2$ of $0.8, 0.7, 0.6$, and 0.5 , respectively.

Diffusing sodium probes (40 000) were generated randomly within the clay dispersions, and their trajectories were simulated independently by using a simple Langevin equation, assuming a single diffusion coefficient ($D_0 = 2 \times 10^{-9} \text{ m}^2/\text{s}$) for the free sodium counterions. However, when a sodium cation hits the clay surface, it remains adsorbed during an average residence time of 50 ps before desorbing and diffusing again into the dispersion. The time step used to integrate the trajectories (20 ps) was selected in order to maintain the individual mean free path smaller than the disk thickness.

The memory function of the quadrupolar coupling was calculated along these trajectories by using a simple two-state model which assumes the coexistence of free and condensed sodium counterions. The characteristic quadrupolar coupling of the free sodium was further assumed to be zero and that of the condensed sodium identified with the residual quadrupolar coupling previously evaluated by molecular modeling⁴⁶ of the clay/water interface ($V_{zz}^{\text{B}} \sim 7 \times 10^{19} \text{ V/m}^2$). The memory functions of the quadrupolar coupling are evaluated as

$$G_m^{\text{D}}(\tau) = (V_{zz}^{\text{B}})^2 \left[\frac{1}{N_i} \sum_{i=1}^{N_i} \sum_{j=1}^{N_p} \sum_{s=1}^{N_p} \sum_{l=-2}^2 P(i \in j|\tau) P(i \in s|0) D_{lm}^{\text{DP}_j} D_{-l-m}^{\text{DP}_s} - \left(\frac{1}{N_i} \sum_{i=1}^{N_i} \sum_{j=1}^{N_p} \sum_{l=-2}^2 P(i \in j|0) D_{lm}^{\text{DP}_j} \right)^2 \right] \quad (16)$$

where N_i is the total number of diffusing ions, N_p the number of clay particles, and $P(i \in j|\tau)$ is the probability that the ion labeled i is adsorbed on the particle labeled j at time τ . As a consequence, in isotropic clay dispersions, the memory function of the quadrupolar coupling was shown to be sensitive to the propagation of the local order^{46,47} induced in the dispersion by the disk/disk excluded volume interactions. By contrast, within nematic dispersions, the memory function of the quadrupolar coupling probed by the diffusing sodium cations is sensitive to the correlations between the fluctuations of the orientation of the clay particles along the nematic director.

III. Results and Discussion

A. Quadrupolar Splitting. Figure 2 displays some example of the variation of the ^{23}Na resonance line as a function of the orientation of the clay dispersion in the magnetic field. The line shape displayed in Figure 2 was analyzed by a complete simulation of the time evolution of the ^{23}Na coherences (see section II.B above) after the single pulse used to produce these NMR spectra. A residual splitting of the resonance line is clearly identified, resulting from the specific orientation of the clay platelets within the dense samples (20.3% w/w). The perfect cancellation of the residual splitting at the so-called magic angle corresponding to the condition $P_2(\cos \theta^{\text{LD}}) = (3 \cos^2 \theta^{\text{LD}} - 1)/2 = 0$ means that all clay particles are aligned along a single macroscopic director, leading to a true macroscopic nematic phase. By contrast, no splitting could be identified at clay concentrations lower than 6.5% w/w, but the analysis of the frequency variation of the ^{23}Na relaxation measurements within such dilute clay dispersions exhibits some local ordering⁴⁷ of the clay platelets.

Since the maximum splitting is detected when the compression axis of the oedemeter used to produce these dense dispersions is aligned parallel to the magnetic field, one may identify the compression axis with the nematic director of the clay dispersion. This maximum residual splitting increases continuously as a function of clay concentration⁴⁵ (see Figure 3), in a much more progressive way than the sharp increase of the order parameter predicted by the numerical simulations of the nematic ordering²² within dispersions of rigid disks. Such a discrepancy may result from some competition between the short-range excluded volume repulsion which favors a parallel alignment of the anisotropic clay particles and the long-range electrostatic repulsion which favors a perpendicular orientation^{39,40} of the charged clay particles. However, the variation of the detected splitting as a function of the clay concentration results from two possible contributions (see eq 6): either the increase of the fraction of condensed sodium counterions or the increase of the degree of nematic ordering. Additional information is thus required to separate the relative impact of both parameters.

B. Line Shape Analysis. Surprisingly enough, this complementary information may also be obtained from ^{23}Na NMR spectroscopy, by exploiting the relaxation behavior of the sodium counterions. This result is somewhat surprising since, as in the case of the residual splitting (cf eq 5), the ^{23}Na relaxation rates measured within these clay dispersions result also from a fast exchange between two spin environments corresponding, respectively, to the free and the condensed sodium counterions

$$R_2^{\text{meas}} = p_{\text{F}} R_2^{\text{F}} + p_{\text{B}} R_2^{\text{B}} \quad (17)$$

with $R_2^{\text{F}} \approx 30 \text{ s}^{-1}$ for sodium in water.⁵⁸ However, information about the nematic order may be extracted from the variation of the transverse relaxation rates as a function of the angle between the static magnetic field and the nematic director of the clay dispersion.

This study focuses on the fast component of the transverse relaxation rate which is responsible for the broadening of the two satellites of the ^{23}Na NMR spectra (see Figure 2). Since the time scale characterizing the loss of memory of the quadrupolar coupling within these dense clay dispersions is much larger⁴⁴ than the inverse of the ^{23}Na resonance angular velocity, the relaxation of the sodium nuclei is performed under the so-called slow modulation regime with a large decrease of the spectral densities between zero and the nominal frequency or twice its value ($J_0^{\text{L}}(0) \gg J_1^{\text{L}}(\omega_0) \approx J_2^{\text{L}}(2\omega_0)$). This slow modulation of the quadrupolar coupling⁴⁴ explains the frequency variation of the ^{23}Na longitudinal relaxation rate measured within clay dispersions.⁴⁴ Because of the large difference between these apparent spectral densities, the broadening of the two satellites is fully driven by a single spectral density $J_0^{\text{L}}(0)$, that is, the integral⁵¹ of the *apparent* memory function $G_0^{\text{L}}(\tau)$ evaluated in the laboratory frame (see section II.B). As shown by eq 14a, this function depends on the orientation of the nematic director of the clay dispersion into the static magnetic field if there is some difference between the three *intrinsic* memory functions of the quadrupolar coupling ($G_m^{\text{D}}(\tau)$, $m = 0, 1, 2$) evaluated in the frame associated with the nematic director of the clay dispersion. Let us first remember that, within isotropic dispersions, the memory functions $G_m^{\text{D}}(\tau)$ are all equal and the apparent relaxation rate is obviously independent of the sample orientation within the static magnetic field.

By the use of the set of eqs 6–15 (see section II.B.3), it is possible to fit *simultaneously* the line shape of the ^{23}Na spectra

measured at various angles between the static magnetic field and the nematic director of the clay sample. As discussed above (see section III.A), the nematic director was shown to coincide with the compression axis used to prepare the dense clay samples. Between 14 and 30 angular values were uniformly selected between -20° and $+120^\circ$. The set of eqs 14–15 is used explicitly to extract the intrinsic spectral densities ($J_m^D(\omega)$) from the angular variation of the apparent spectral densities ($J_m^L(\omega)$). A numerical procedure⁶⁵ is used to simultaneously fit the corresponding spectra by minimizing the sum of the squared deviations between each simulated and experimental spectrum. The fitted parameters are the maximum apparent quadrupolar splitting (ω_0^{MAX}) detected at $\theta^{\text{LD}} = 0^\circ$ and the intrinsic spectral densities $J_0^D(0)$, $J_1^D(0)$, $J_2^D(0)$, $J_0^D(\omega_0)$, and $J_1^D(\omega_0)$. To maintain the number of fitted parameters as small as possible, we assumed that the spectral densities at twice the nominal frequency coincide with their value at the nominal frequency

$$J_m^D(2\omega_0) = J_m^D(\omega_0) \quad (18)$$

for $m = 0, 1$, and 2 . This approximation is validated by the large differences between the spectral densities evaluated at zero frequency and the same spectral densities evaluated at the nominal frequency or twice its value. We further reduced the number of fitted parameters by assuming

$$J_2^D(\omega_0) = \frac{J_2^D(0)}{J_1^D(0)} J_1^D(\omega_0) \quad (19)$$

whose validity will be discussed later. Figure 2 illustrates some results obtained for a clay concentration 20.3% (w/w). The corresponding angular variation of the ^{23}Na apparent spectral density ($J_0^L(0)$), which represents the major contribution to the fast component of the transverse relaxation rate (R_2^{fast}), is displayed in Figure 4 in addition to the contributions from its intrinsic spectral densities ($J_m^D(0)$, with $m = 0-2$).

As shown in Figure 5, the intrinsic spectral density $J_2^D(0)$, which is a priori proportional to the fraction of condensed sodium counterions, remains around 10^4 s^{-1} in the whole range of clay concentration. This result is consistent with a constant fraction of condensed sodium counterions in this range of clay concentration, in agreement with the prediction of the condensation theory.^{66–67} By contrast, the intrinsic spectral densities $J_0^D(0)$ and $J_1^D(0)$ are roughly equivalent and increase gradually as a function of clay concentration, reaching a value of $4 \times 10^4 \text{ s}^{-1}$ at the highest clay concentration. Let us remember that, within isotropic dispersions, these three intrinsic spectral densities coincide. As a consequence, the difference between the intrinsic spectral densities is a fingerprint of the organization of the clay particles within these dense dispersions. Thus, because of the stability of the fraction of condensed sodium counterions in this concentration range, the gradual increase of the difference between the two spectral densities ($J_0^D(0) - J_2^D(0)$) is interpreted as an intrinsic fingerprint of the organization of the clay dispersion and results from a gradual increase of the degree of nematic ordering in this range of clay concentration. As a consequence, in the whole range of clay concentration, Figure 6 exhibits a linear correspondence between the variation of the maximum quadrupolar splitting and that of the difference between the spectral densities ($J_0^D(0) - J_2^D(0)$). However, numerical simulations are required to understand how the organization of the clay particle can affect the intrinsic spectral densities and explain the origin of their difference.

C. Hahn Echo Attenuation. Due to the possible contributions of the heterogeneities of the static magnetic field, the line shape analysis is not the best procedure to extract the apparent spectral densities. We have thus measured the attenuation of the echo during the Hahn pulse sequence which compensates for the contribution from the magnetic field heterogeneities. As for the line shape analysis, the echo attenuation is measured at different angles between the static magnetic field and the sample director. Here, between 14 and 30 angular values are uniformly selected between -20° and $+120^\circ$ as well. These echo attenuations are simultaneously fitted by solving the set of eqs 6–15 for the Hahn pulse sequence (see section II.B.3). The same fitting procedure⁶⁵ is used to extract the same set of parameters (see section III.B). Figure 7 displays some angular variation of the echo attenuation and the corresponding fitted data. As shown in Figures 5 and 6, the results are fully compatible with the data obtained from the line shape analysis, validating that procedure. Because of the large value of the apparent relaxation rate of the two satellites ($R_2^{\text{fast}} \sim 10^4 \text{ s}^{-1}$), one may understand that the magnetic field heterogeneities remain negligible.

A question remains, however, to be settled: All these data were obtained by assuming a single quadrupolar splitting for the condensed sodium counterions. If various environments coexist, we assume a fast exchange between the different spin populations leading to a single, detectable spin environment. This hypothesis is compatible with the temperature variation of the longitudinal relaxation rate previously measured⁴⁴ for these aqueous clay dispersions. Furthermore, if various environments of the quadrupolar nuclei coexist in the slow exchange regime, the principal axis of their quadrupolar tensor must all be aligned along the same director, otherwise no magic angle will be detected (see Figures 2 and 7). Nevertheless, a distribution of the amplitude of the quadrupolar coupling may still occur and explain the large difference between the apparent spectral density ($J_0^L(0)$) extracted from the transverse relaxation of the two satellites by comparison with the two spectral densities ($J_1^L(\omega_0)$ and $J_2^L(2\omega_0)$) monitoring the transverse relaxation of the central line. However, measurements of the longitudinal relaxation time in the rotating frame ($T_{1\rho}$) were already performed within such nematic clay dispersions.⁴⁴ The data exhibit a continuous variation of the apparent spectral density ($J_0^L(\omega)$) at angular velocity ranging between 10^5 and 10^6 s^{-1} (see Figure 9 in ref 44). Furthermore, at the lowest accessible angular velocity, the apparent spectral density ($J_0^L(\omega)$) reaches the order of magnitude of the apparent spectral density ($J_0^L(0)$) evaluated from the transverse relaxation rate of the two satellites. As a consequence, the large value of the apparent spectral density ($J_0^L(0)$) does not result from a distribution of the residual quadrupolar coupling, but it is the consequence of the dynamical properties of the ^{23}Na quadrupolar nuclei that diffuse in the space limited by the charged anisotropic clay particles.

D. Numerical Simulations. Because of the complexity of the system under study, numerical simulations are necessary to understand the interplay between ion diffusion and relaxation and the structure of the clay dispersion. To illustrate the influence of the degree of nematic ordering on the orientational variation of this relaxation rate, we have performed a set of numerical simulations of the sodium counterions diffusion and relaxation by varying the degree of nematic ordering of the clay dispersion (see section II.C). Figure 8 exhibits the memory functions of the three components of the quadrupolar coupling ($G_m^D(\tau)$, $m = 0, 1$, and 2) evaluated in the frame associated with the nematic director for the two limiting cases corresponding

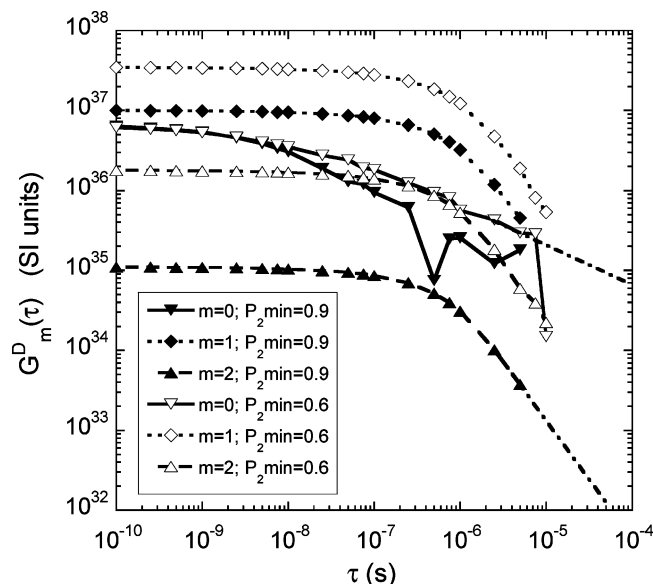


Figure 8. Influence of the degree of ordering predicted by numerical simulation of the memory functions describing the decorrelation of the quadrupolar coupling in a frame attached to the clay dispersion (see text).

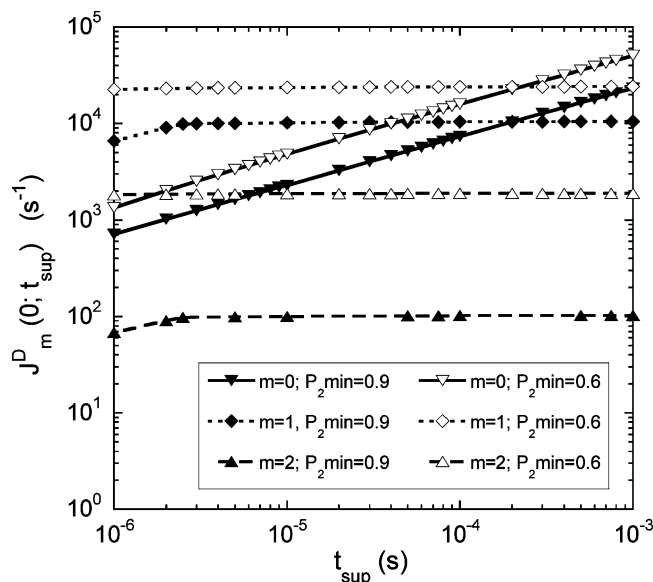


Figure 9. Intrinsic spectral densities evaluated in the frame attached to the clay dispersion and resulting from the integration of the memory functions displayed in Figure 8.

to the most ordered ($P_2^{\min} = (3(\cos \theta_{\min}^{\text{DP}})^2 - 1)/2 = 0.9$) and the less ordered ($P_2^{\min} = (3(\cos \theta_{\min}^{\text{DP}})^2 - 1)/2 = 0.6$) clay dispersions, respectively. One first note, a drastic change occurs between the long-time asymptotic behavior of these memory functions which decrease slowly according to a $\tau^{-0.5}$ power law for the $m = 0$ component and according to a $\tau^{-1.5}$ power law for the two other components. While the second behavior is classic for a relaxation mechanism induced by 3D diffusion, the first behavior corresponds to 1D diffusion and leads to a pathological divergence of the corresponding spectral density $J_0^{\text{D}}(0)$. This point will be discussed later. The ordering has no drastic impact on the memory function $G_0^{\text{D}}(\tau)$ but simply shifts the occurrence of its asymptotic behavior to shorter times, thus slightly reducing the corresponding spectral density (see $J_0^{\text{D}}(0)$ in Figure 9). By contrast, the $m = 1$ component ($G_1^{\text{D}}(\tau)$) is significantly reduced by the degree of ordering of the nematic

dispersion, while the $m = 2$ component ($G_2^{\text{D}}(\tau)$) is decreased by more than 1 order of magnitude. As a consequence, one expects to detect a marked increase of the difference between the corresponding spectral densities ($J_0^{\text{D}}(0) \gg J_2^{\text{D}}(0)$) as a function of the degree of ordering of the dispersion.

Due to the perfect parallelism between the time evolution of the memory function $G_m^{\text{D}}(\tau)$ for $m = 1$ and 2 (see Figure 8) or equivalently the perfect parallelism between the intrinsic spectral densities $J_m^{\text{D}}(\omega)$ for $m = 1$ and 2 (see Figure 9), one may be very confident in the validity of the hypothesis expressed in eq 19 and used to reduce the number of fitted parameters.

A question remains, however, to be settled: the divergence of the spectral density $J_0^{\text{D}}(0)$ because of the power law exhibited by the memory function $G_0^{\text{D}}(\tau)$. One may first argue that this problem results from the oversimplification of the two-state model used to analyze the diffusion and relaxation of the sodium counterions within such nematic dispersion of charged clay particles. A more realistic treatment is now in progress by including the contribution of the diffuse layer into the force field responsible for the cation trajectories and the derivation of its electrostatic field gradient responsible for the quadrupolar relaxation. Nevertheless, this divergence is not redhibitory but simply invalidates the replacement by infinity of the upper limit of the integral⁵¹ in eq 8 (see section II.B). To allow for some comparison between the different contributions to the apparent relaxation rate of the two satellites (i.e., mainly $J_0^{\text{D}}(0)$), Figure 9 displays the two spectral densities $J_m^{\text{D}}(0)$ easily integrated for $m = 1$ and 2 and the only defined quantity

$$J_0^{\text{D}}(0; t_{\text{sup}}) = 6C_Q^2 \int_0^{t_{\text{sup}}} G_0^{\text{D}}(\tau) d\tau \quad (20)$$

which is integrated over the time scale of interest for the fast relaxation of the two satellites. This integration domain varies between 1 and $10^3 \mu\text{s}$ corresponding, respectively, to the time step used for the FID acquisition, as a lower limit (cf. section II.B), and three times the inverse of the fastest relaxation rate, as an upper limit. As displayed by Figure 9, in that time scale, the effective contribution to the fast relaxation rate induced by $J_0^{\text{D}}(0; t_{\text{sup}})$ reaches the same order of magnitude as the contribution from $J_1^{\text{D}}(0)$, while that originating from $J_2^{\text{D}}(0)$ becomes more and more negligible as a function of the degree of nematic ordering of the dispersion.

These numerical simulations also reveal the limitations of the simple analysis of the relaxation measurements based on the two-state model (cf. eq 17) since the relaxation rate characterizing the condensed sodium counterions (R_2^{B}) is not an absolute constant but it depends also on the organization of the clay dispersion. Numerical simulations of the ionic diffusion are thus required to determine the correlation between the relaxation of the counterions and the structure of the clay dispersion in which ionic diffusion occurs. Despite the simplicity of the two-state model used for these numerical simulations of Brownian dynamics, the predicted spectral densities (cf. Figure 9) match the order of magnitude of the measured relaxation rates. More detailed simulations are now under progress and implicitly include the contribution from the electrostatic potential around the charged colloids in order to obtain more quantitative predictions.

As a conclusion, information on the degree of nematic ordering within the clay dispersion will be obtained if we are able to extract from the apparent fast relaxation rates (i.e., from $J_0^{\text{D}}(0)$) the order of magnitude of the intrinsic spectral densities⁴⁸ evaluated in the frame attached to the dispersion (i.e.,

$J_m^D(0)$, $m = 0-2$). This is performed by measuring the variation of the apparent relaxation rates of the two satellites as a function of the orientation of the sample into the magnetic field (cf. eq 14a).

By analyzing Figures 3 and 5, one can note some parallelism between the maximum quadrupolar splitting (ω_Q^{MAX}) and the intrinsic spectral density $J_m^D(0)$. Figure 6 directly illustrates this parallelism, despite some uncertainties. Since the intrinsic spectral density $J_2^D(0)$ is independent of the clay concentration, one can conclude that the fraction of condensed sodium counterions remains constant in the range of clay concentration. As a consequence, the increase of the difference between the two intrinsic spectral densities ($J_0^D(0) - J_2^D(0)$) as a function of the quadrupolar splitting results from the progressive nematic ordering within this range of clay concentrations. This gradual increase of the organization of the clay dispersion is more progressive than that reported from numerical simulations of the isotropic/nematic transition of rigid disks.²² A possible interpretation is the strong reduction of the effective²¹ aspect ratio of our charged colloids because of the thickness of the diffuse layers²¹ of counterions condensed on the basal surfaces of the clay. Previous numerical simulations of the influence of the electrostatic coupling on the stability of two charged disks immersed in a large simulation cell have also demonstrated that the electrostatic repulsion between two charged disks perpendicular⁴¹ to each other was significantly smaller than that between two parallel disks, even in the presence of a large excess of salt. As a consequence, the very progressive ordering detected by ²³Na NMR spectroscopy within dense aqueous dispersions of Laponite clay results from a competition between their long-range electrostatic coupling and short-range excluded volume repulsion. It should be interesting to continue this investigation by increasing the size and modifying the shape of the charged colloids in order to determine the conditions under which the behavior of the dispersion becomes totally driven by the excluded volume interactions.

IV. Conclusions

²³Na NMR spectroscopy is used to detect the nematic ordering within dense dispersions of synthetic clay, a model of charged anisotropic colloids. The progressive increase of the residual quadrupolar splitting detected as a function of the clay concentration may result from two simultaneous phenomena: an increase of the fraction of condensed sodium counterions and a gradual improvement of the degree of nematic ordering within the clay dispersion. By a simultaneous analysis of the line shape recorded by ²³Na NMR spectroscopy and the echo attenuation during an Hahn pulse sequence, it was possible to extract the intrinsic relaxation rates evaluated in the frame of the nematic director from the angular variation of the apparent relaxation rates. As illustrated by numerical simulations of the ion diffusion and relaxation, the difference between these intrinsic relaxation rates is a qualitative probe of the degree of ordering of the clay dispersion. This procedure may be extended to any dispersion of charged anisotropic particles (mineral colloids, polyelectrolytes, biological macromolecules) of any shape (cylinders, disks, ellipsoids) neutralized by quadrupolar counterions (⁷Li, ²³Na, ⁸⁷Rb).

Acknowledgment. We cordially thank Drs J. van der Maarel, P. Levitz, J. Puibasset, L. Michot, and A.L. Rollet for helpful discussions. The Bruker spectrometer was purchased thanks to a grant from the Région Centre (France). The numerical simulations were performed either at the Gage

Computing Facilities (Palaiseau, France) or locally on workstations purchased thanks to grants from the Région Centre (France).

References and Notes

- (1) Mouchid, A.; Delville, A.; Lambard, J.; Lécolier, E.; Levitz, P. *Langmuir* **1995**, *11*, 1942.
- (2) Gabriel, J. C. P.; Sanchez, C.; Davidson, P. *J. Phys. Chem. B* **1996**, *100*, 11139.
- (3) Lemaire, B. J.; Panine, P.; Gabriel, J. C. P.; Davidson, P. *Europhys. Lett.* **2002**, *59*, 55.
- (4) O'Brien, S.; Tudor, J.; O'Hare, D. *J. Mater. Chem.* **1999**, *9*, 1819.
- (5) Saunders, J. M.; Goodwin, J. W.; Richardson, R. M.; Vincent, B. *J. Phys. Chem. B* **1999**, *103*, 9211.
- (6) Levitz, P.; Lécolier, E.; Mouchid, A.; Delville, A.; Lyonnard, S. *Europhys. Lett.* **2000**, *49*, 672.
- (7) Leach, E. S. H.; Hopkinson, A.; Franklin, K.; van Duijneveldt, J. S. *Langmuir* **2005**, *21*, 3821.
- (8) Wierenga, A.; Philipse, A. P.; Lekkerkerker, H. N. W.; Boger, D. V. *Langmuir* **1998**, *14*, 55.
- (9) Pelletier, O.; Davidson, P.; Bourgaux, C.; Coulon, C.; Regnault, S.; Livage, J. *Langmuir* **2000**, *16*, 5295.
- (10) van der Kooij, F. M.; van der Beek, D.; Lekkerkerker, H. N. W. *J. Phys. Chem. B* **2001**, *105*, 1696.
- (11) Bihannic, I.; Michot, L. J.; Lartiges, B. S.; Vantelon, D.; Labille, J.; Thomas, F.; Susini, J.; Salomé, M.; Fayard, B. *Langmuir* **2001**, *17*, 4144.
- (12) Van der Beek, D.; Lekkerkerker, H. N. W. *Europhys. Lett.* **2003**, *61*, 702.
- (13) Purdy, K. R.; Fraden, S. *Phys. Rev. E* **2004**, *70*, 061703.
- (14) Caggioni, M.; Roshi, A.; Barjami, S.; Mantegazza, F.; Iannacchione, G. S.; Bellini, T. *Phys. Rev. Lett.* **2004**, *93*, 12801.
- (15) Camerel, F.; Gabriel, J. C. P.; Batail, P.; Panine, P.; Davidson, P. *Langmuir* **2003**, *19*, 10028.
- (16) Michot, L. J.; Bihannic, I.; Porsch, K.; Maddi, S.; Bavarian, C.; Mougél, J.; Levitz, P. *Langmuir* **2004**, *20*, 10829.
- (17) Wang, G. F.; Lai, S. K. *Phys. Rev. E* **2004**, *70*, 051402.
- (18) Jagadeesh, B.; Prabhakar, A.; Ramana Rao, M. H. V.; Murty, C. V. S.; Pisipati, V. G. K. M.; Kunwar, A. C.; Bowers, C. R. *J. Phys. Chem. B* **2004**, *108*, 11272.
- (19) Ozturk, B.; Behin-Aein, G.; Flanders, B. N. *Langmuir* **2005**, *21*, 4452.
- (20) Mohraz, A.; Solomon, M. J. *Langmuir* **2005**, *21*, 5298.
- (21) Forsyth, P. A.; Marcelja, S., Jr.; Mitchell, D. J.; Ninham, B. W. *Adv. Colloid Interface Sci.* **1978**, *9*, 37.
- (22) Eppenga, R.; Frenkel, D. *Mol. Phys.* **1984**, *6*, 1303.
- (23) Savenko, S. V.; Dijkstra, M. *Phys. Rev. E* **2004**, *70*, 051401.
- (24) Odriozola, G.; Romero-Bastida, M.; Guevara-Rodríguez, F. de J. *Phys. Rev. E* **2004**, *70*, 021405.
- (25) Shundyak, K.; van Roij, R. *Phys. Rev. E* **2004**, *69*, 041703.
- (26) Bellier-Castella, L.; Caprion, D.; Ryckaert, J. P. *J. Phys. Chem. B* **2004**, *121*, 4874.
- (27) Sokolowska, D.; Moscicki, J. K. *Phys. Rev. E* **2005**, *71*, 031701.
- (28) Boublik, T. *J. Phys. Chem. B* **2004**, *108*, 7424.
- (29) Barnard, A. S.; Zapol, P. *J. Chem. Phys.* **2004**, *121*, 4276.
- (30) Cinacchi, G.; De Gaetani, L.; Tani, A. *J. Chem. Phys.* **2005**, *122*, 184513.
- (31) Decruppe, J. P.; Lerouge, S.; Azzouzi, H. *Phys. Rev. E* **2005**, *71*, 011503.
- (32) Nettesheim, F.; Grillo, I.; Lindner, P.; Richtering, W. *Langmuir* **2004**, *20*, 3947.
- (33) Van der Beek, D.; Schilling, T.; Lekkerkerker, H. N. W. *J. Chem. Phys.* **2004**, *121*, 5423.
- (34) Van der Beek, D. Ph.D. Thesis, University of Utrecht, Holland, April 2005.
- (35) Kimura, F.; Kimura, T.; Tamura, M.; Hirai, A.; Ikuno, M.; Horii, F. *Langmuir* **2004**, *21*, 2034.
- (36) Cardon, Th. B.; Dave, P. C.; Lorigan, G. A. *Langmuir* **2005**, *21*, 4291.
- (37) Kimura, T.; Yoshino, M. *Langmuir* **2005**, *21*, 4805.
- (38) Onsager, L. *Ann. N. Y. Acad. Sci.* **1949**, *51*, 627.
- (39) Delville, A. *Langmuir* **2003**, *19*, 7094.
- (40) Dijkstra, M.; Hansen, J. P.; Madden, P. A. *Phys. Rev. E* **1997**, *55*, 3044.
- (41) Meyer, S.; Levitz, P.; Delville, A. *J. Phys. Chem. B* **2001**, *105*, 10684.
- (42) Thompson, D. W.; Butterworth, J. T. *J. Colloid Interface Sci.* **1992**, *151*, 236.
- (43) Balnois, E.; Durand-Vidal, S.; Levitz, P. *Langmuir* **2003**, *19*, 6633.
- (44) Porion, P.; Al-Mukhtar, M.; Meyer, S.; Faugère, A. M.; van der Maarel, J. R. C.; Delville, A. *J. Phys. Chem. B* **2001**, *105*, 10505.

- (45) Porion, P.; Al-Mukhtar, M.; Faugère, A. M.; Delville, A. *J. Phys. Chem. B* **2004**, *108*, 10825.
- (46) Porion, P.; Faugère, M. P.; Lécolier, E.; Gherardi, B.; Delville, A. *J. Phys. Chem. B* **1998**, *102*, 3477.
- (47) Delville, A.; Porion, P.; Faugère, A. M. *J. Phys. Chem. B* **2000**, *104*, 1546.
- (48) Barbara, Th. M.; Vold, R. R.; Vold, R. L. *J. Chem. Phys.* **1983**, *79*, 6338.
- (49) Dubois, M.; Zemb, Th.; Belloni, L.; Delville, A.; Levitz, P.; Setton, R. *J. Chem. Phys.* **1992**, *96*, 2278.
- (50) Delville, A. *J. Phys. Chem. B* **2002**, *106*, 7860.
- (51) Abragam, A. *The Principles of Nuclear Magnetism*; Clarendon Press: Oxford, U.K., 1961.
- (52) Kimmich, R. *NMR Tomography, Diffusometry, Relaxometry*; Springer: Berlin, Germany, 1997.
- (53) Hancu, I.; van der Maarel, J. R. C.; Boada, F. E. *J. Magn. Reson.* **2000**, *147*, 179.
- (54) van der Maarel, J. R. C.; Jesse, W.; Hancu, I.; Woessner, D. E. *J. Magn. Reson.* **2001**, *151*, 298.
- (55) van der Maarel, J. R. C.; Woessner, D. E.; Merritt, M. E. *J. Phys. Chem. B* **2002**, *106*, 3864.
- (56) van der Maarel, J. R. C. *Concepts Magn. Reson. A* **2003**, *19*, 97.
- (57) van der Maarel, J. R. C. *Concepts Magn. Reson. A* **2003**, *19*, 117.
- (58) Hertz, H. G. *Ber. Busen-Ges. Phys. Chem.* **1973**, *77*, 531.
- (59) Müller, N.; Bodenhausen, G.; Ernst, R. R. *J. Magn. Reson.* **1987**, *75*, 297.
- (60) Jaccard, G.; Wimperis, S.; Bodenhausen, G. *J. Chem. Phys.* **1986**, *85*, 6282.
- (61) Kemp-Harper, R.; Brown, S. P.; Hughes, C. E.; Styles, P.; Wimperis, S. *Prog. Nucl. Reson. Spectrosc.* **1997**, *30*, 157.
- (62) Quist, P. O.; Halle, B. *Phys. Rev. E* **1993**, *47*, 3374.
- (63) Trouard, Th. P.; Alam, T. M.; Brown, M. F. *J. Chem. Phys.* **1994**, *101*, 5229.
- (64) Separovic, F.; Cornell, B.; Pace, R. *Chem. Phys. Lipids* **2000**, *107*, 159.
- (65) Deming, S. N.; Morgan, S. L. *Anal. Chem.* **1973**, *45*, 278A.
- (66) Oosawa, F. *J. Polym. Sci.* **1957**, *23*, 421.
- (67) Manning, G. S. *Acc. Chem. Res.* **1979**, *12*, 443.